Limits of the potential flow approach to the single-mode Rayleigh-Taylor problem

P. Ramaprabhu[(1)], Guy Dimonte[(1)], Yuan-Nan Young[(2)], Alan C. Calder[(3)], Bruce Fryxell[(4)]

[(1)] Center for Nonlinear Studies
Los Alamos National Laboratory
Los Alamos, New Mexico, 87545

[(2)] Department of Mathematical Sciences
New Jersey Institute of Technology
Newark, New Jersey, 07102

[(3)] ASCI/FLASH Center
University of Chicago
Chicago, IL, 60637

[(4)] Aerospace Engineering Department
Georgia Institute of Technology
Atlanta, GA 30332

CAMS Report 0506-16, Spring 2006

Center for Applied Mathematics and Statistics

NJIT

Limits of the potential flow approach to the single-mode Rayleigh-Taylor problem

P. Ramaprabhu[a], Guy Dimonte
Los Alamos National Laboratory

Yuan-Nan Young
New Jersey Institute of Technology

A.C. Calder
University of Chicago

B. Fryxell
Georgia Tech

Abstract

We report on the behavior of a single-wavelength Rayleigh-Taylor flow at late-times. The calculations were performed in a long square duct ($\lambda x \lambda x 8\lambda$), using four different numerical simulations. In contradiction with potential flow theories that predict a constant terminal velocity, the single-wavelength Rayleigh-Taylor problem exhibits late-time acceleration. The onset of acceleration occurs as the bubble penetration depth exceeds the diameter of bubbles, and is observed for low and moderate density differences. We provide a phenomenological description of the observed acceleration, and ascribe this behavior to the formation of Kelvin-Helmholtz vortices on the bubble-spike interface that diminish the friction drag. For large density ratios, the formation of secondary instabilities is suppressed, and the bubbles remain terminal consistent with potential flow models.

PACS number: 47.20.Bp.

[a)] Center for Nonlinear Studies

I. Introduction

The acceleration of a fluid in to a second fluid of greater density ($\rho_2 > \rho_1$)constitutes a Rayleigh-Taylor (RT) instability[1], a problem of significance to the Inertial Confinement process[2], and supernovae formation[3]. Small perturbations of amplitude h_0 and wavenumber k at the interface between the fluids grow exponentially in time until kh_0~1:

$$h(t) = h_0 \cosh(\Gamma t) \qquad (1)$$

In the absence of surface-tension, viscosity or other mitigating effects, the associated growth rate[4] from (1) is $\Gamma = \sqrt{Agk}$, where g is the acceleration and the Atwood number $A = \frac{\rho_2 - \rho_1}{\rho_2 + \rho_1}$ parameterizes the density difference between the fluids. At larger amplitudes, the flow is differentiated in to *bubbles* of light fluid penetrating the heavy, and *spikes*, which are fingers of the heavy fluid descending in to the light fluid. Drag-buoyancy[5] models and potential flow theory[6] predict that for $kh_0 > 1$, the perturbations undergo a nonlinear saturation toward a terminal bubble velocity given by

$$v_b = Fr\sqrt{Ag\lambda/(1+A)}, \qquad (2)$$

where Fr is the bubble Froude number. Numerical simulations[7] have shown that (2) holds for bubbles for all A, with Fr = 0.56 for a square mode initial perturbation. The models also give corresponding expressions for spike behavior, although at large density differences, spikes do not stay terminal, instead approaching free-fall ($h_s \sim Agt^2$). Thus, bubble and spike growths are identical at small A, but diverge as $A \rightarrow 1$.

This simple picture of single-wavelength growth is significant because it can be extended through dimensional arguments to improve our understanding of the turbulent RT. Indeed, the so-called bubble competition[8] models treat dominant bubbles in a chaotic bubblefront, as essentially 'single-modes' isolated from the effects of neighbors. Such dominant bubbles grow self-similarly with their diameter $D_b \sim h_b$, according to experiments and simulations. Thus, replacing D_b with h_b for leading bubbles in (2), we get

$$h_b = \alpha A g t^2, \qquad (3)$$

where α is the growth rate of the RT mix envelope. It has been shown first for the beam-plasma instability and then for RT[8] that the dominant wavepacket at a given time may be treated as a single-mode by substituting the r.m.s. amplitude of modes in that wavepacket for the single-mode amplitude, up to an autocorrelation time after saturation. For the turbulent RT, transition to nonlinearity occurs when the r.m.s. amplitude of the wavepacket, rather than the amplitude of individual modes, exceeds *1/k*.

In the spirit of the above discussion, equations (2) and (3) may be combined to give

$$\alpha = \frac{Fr^2}{8}\frac{\rho_1 + \rho_2}{\rho_2}\frac{D_b}{h_b}, \qquad (4)$$

but a value of $Fr \sim 1$, higher than the single-mode value, is required to match experimentally measured values of α and D_b/h_b, as described by [9], [10] and [11]. Analysis of leading bubbles from numerical simulations and experiments that accounts for the entrainment of the heavier fluid by bubbles, confirm this higher value of *Fr*. Thus, leading bubbles in a turbulent flow resemble the isolated buoyant plumes of Scorer's

experiment[12] (Fr = 1.1), rather than an array of tightly packed bubbles (Fr = 0.56). Such isolated plumes/bubbles have an increased Fr due to reduced counterflow drag from spike flow surrounding the bubbles – as the area separating neighboring bubbles is increased, the spike velocity is diminished due to mass conservation. This is evident in the experiments of [13], who observed an increase in the value of Fr of a lenticular bubble from ½ to 2/3, as the walls of the container were moved away. Similarly, the observed aspect ratios (D_b/h_b) of turbulent RT bubbles range from 1/3 to 2/3, in contrast to the single-mode value of ~ 1.

Thus, the single-mode description of leading bubbles in turbulent RT is promising, but must be revised towards a higher Fr and lower D_b/h_b. Experiments and simulations of single-wavelength RT flows[7,14] have focused on bubble evolution at early and intermediate times. In this paper, we use 3D numerical simulations to study the late-time single-mode RT problem in a regime of relevance to the turbulent flow, i.e. large Fr and small D_b/h_b. Under these conditions, the single-wavelength flow much to our surprise, exhibits deviations from the expected terminal velocity. Bubbles (and spikes at low A) accelerate before saturating to a Fr ~ 1, closer to the turbulent value. We provide a phenomenological description of our observations, and an explanation for the late-time bubble acceleration.

II. Numerical Techniques and Problem Setup

The numerical algorithms used in this study have been described in detail in [15], and only a brief overview is provided here. Three of the numerical codes used the MILES (Monotone Integrated Large Eddy Simulation) technique, while the fourth was a Direct Numerical Simulation (DNS). RTI-3D[16] is a multi-phase, incompressible, Eulerian solver and uses Van Leer flux limiters to prevent non-physical oscillations. FLASH[17] and PROMETHEUS[18] solve the compressible Euler equations using the Piecewise Parabolic Method on a 3D Cartesian grid. FLASH is a parallel code and has the added feature of Adaptive Mesh Refinement, handled by the PARAMESH[19] library of routines. NAV/STK is a finite-volume solver for the full Navier-Stokes equations with a physical viscosity, in addition to the capability to handle surface tension effects. The MILES algorithm has an implicit viscosity due to subgrid smoothing of fine-scales that may be written from dimensional arguments[15] as

$$\nu \sim \sqrt{Ag\Delta^3}\,, \qquad (5)$$

where Δ is the zone size. It has been demonstrated that the numerical viscosity in these codes behaves much like a physical viscosity, not only giving the correct linear growth rates (modified by viscosity), but accurately predicting the Kolmogorov cutoff wavenumber in turbulent calculations[15]. Table 1 provides a summary of the numerical techniques discussed above.

The three-dimensional simulations were initialized with a square-mode initial perturbation of amplitude h_0 and wavenumber k, of the form

$$h(x, y) = h_0 \{\cos(kx) + \cos(ky)\}. \qquad (6)$$

This form of the perturbation places the bubble at the center of the computational domain, while the spikes are placed at the corners. The perturbation amplitudes were chosen to be such that $kh_0 << 1$. To study the late-time behavior of RT, the perturbations were set up in a long, square duct (λxλx8λ), with periodic boundary conditions in the lateral directions, and no-flow boundary conditions in the direction of gravity. The perturbation wavelengths, Atwood numbers used, and grid resolutions employed in the codes are listed in Table 2. The compressible codes were run in a nearly incompressible limit, with an adiabatic condition[15] for the vertical density profile to approximate hydrostatic equilibrium. The background pressure is chosen to be 500 dynes/cm^2, limiting the vertical density variation to less than 6%.

III. Computational Results

Figures 1 and 2 are contour plots of density ($\frac{\rho_1 + \rho_2}{2}$) from RTI-3D and NAV/STK simulations at A = 0.5 and 0.2 respectively. The panel (a) is at early-time while (b) is towards the end of the simulation. The realizations are in a plane passing through the center of the bubble, while the spikes are located outside this plane and near the corners of the box. The time-histories of bubble amplitude and velocity from RTI-3D are shown in figures 3 (a) and (b) respectively at A = 0.5. For h_b/D_b <1, bubble velocities are constant and in agreement with (2). As bubbles exceed this aspect ratio, they accelerate, before appearing to saturate late in time to a constant velocity.

Figure 4 is a plot of the corresponding Fr for $kh_b > 1$ and $h_b < D_b$, for different A, from the MILES and DNS codes, and shows agreement with the drag-buoyancy[5] and potential

flow[6] type models. Note that the models assume a Bessel function for the initial interfacial perturbation, while our calculations are initialized with a square-mode. This difference in the form of the perturbation does not lead to a discrepancy in the results. In this regime, bubbles have a *Fr* of 0.56, independent of *A*. For bubbles, balancing the buoyancy and drag forces gives

$$\ddot{h}_b = Ag - C\dot{h}_b^2 \frac{\rho_2}{\rho_1 + \rho_2} \frac{Area}{Volume}, \qquad (7)$$

where *C* is a drag coefficient. Choosing $C \sim 2\pi$ as suggested by [5], $Area/Volume \sim 1/D_b$, and setting $h_b'' = 0$, we obtain (2) for v_b. This simple model ignores the late-time onset of secondary instabilities in the form of Kelvin-Helmholtz rollups at low *A*, and bubble-spike coupling at high *A*. A similar force balance analysis for spikes reveals identical spike behavior at low A. However, for $A > 0.5$, the drag forces due to bubbles vanish, causing the spikes to accelerate[7], ultimately approaching free-fall ($h_s = \frac{1}{2} gt^2$) as $A \rightarrow 1$.

According to figure (3), equation (7) describes the bubble behavior only up to intermediate times, but not the late-time acceleration and subsequent velocity saturation. This deviation from (7) is observed consistently in all of the numerical simulations shown in figure 5, which is a plot of the Froude number variation with bubble aspect ratio (h_b/D_b). Furthermore, the simulations consistently show that the onset of bubble acceleration is at $h_b/D_b \sim 1$, and that bubbles ultimately saturate to $Fr \sim 1$. We note that in all the codes, this behavior is observed for $A < 0.75$, and not at higher density differences. This is evident from the $A = 0.9$ case shown in figure (5), which does not show any bubble acceleration late in time. A complete discussion of this Atwood number effect is

deferred until § IV. The marker arrows in figure 5 point to the turbulent values of *Fr* and h_b/D_b, obtained from simulations and experiments, for comparison.

Such late-time non-stationary behavior of single-mode RT spikes and bubbles were observed and reported in [20], who ascribe the deviation from steady-state, to changes in the tip curvature of bubbles and spikes. We argue in the following that it is the formation of secondary instabilities, rather than the curvature of the bubble/spike tip that describes the observed behavior. The onset of bubble oscillations may also be observed at late-time in the 2D DNS of [21]. Finally, 2D and 3D numerical simulations using the MAH-3 code[22] also show an increase of bubble velocities at late-time. The 2D NS of [20] suggest a strong correlation between bubble/spike curvature and their velocity variations. While the bubbles appear more pointed after the onset of acceleration in figure 1, the change in shape is less dramatic in the DNS calculations shown in figure 2. Thus, it is not evident if the bubbletip curvature is a determinant of the observed behavior reported here.

To eliminate numerics as a possible explanation of our observations, several tests were performed on the codes. Firstly, the size of the domain was doubled to determine end wall effects, if any. Secondly, the MILES calculations were repeated at a higher resolution to reduce the effective numerical viscosity. Both these studies reproduced the results described above: Saturation velocity for $h_b/D_b < 1$ and bubble acceleration at late times. Finally, a numerical experiment was performed in which a buoyant spherical bubble was allowed to rise in a large container. The experiments of [13] report a constant value for the Froude number of a lenticular bubble of 2/3. Our simulations show a similar

behavior, as the bubble rose self-similarly with a nearly constant Fr of 0.8. This suggests that the late-time acceleration observed for the RT bubble is not a result of numerical artifacts.

This acceleration of bubbles has not been reported in experiments of single-mode RT, since most experiments report bubble velocities up to $h_b/D_b \sim 1$. Planar Laser Induced Fluoresence (PLIF) images from the drop-tank experiments of [14], show bubbles which appear square with an aspect ratio close to unity. The closest experimental analog to our calculations is the study of rising air bubbles in a long tube filled with water[13]. The authors of that paper who were interested in the question of how long it would take to empty such a tube of liquid, report a constant $Fr \sim 0.46$ for the rising column of air. However, those experiments were at $A = 1$, a regime in which we do not observe any acceleration either. Since these experiments had surface-tension effects, some of the high Atwood number DNS calculations were repeated with the addition of surface tension. These calculations showed only a slight decrease in the bubble acceleration with the inclusion of surface tension. We conclude this section by pointing out the need for single-mode RT experiments to study the late-time behavior of bubbles and spikes at all Atwood numbers.

IV. Discussion: Effect of secondary instabilities

The drag coefficient C in (7) includes the effects of form and friction drag of bubbles on spikes and vice-versa. For instance, for a bluff object in wind tunnel flow, the total drag force may be written as[23]

$$F = \left\{ C_{form} \frac{D_b}{h_b} + 4C_{friction} \frac{h_b}{D_b} \right\} h_b'^2 \frac{\rho_2}{\rho_1 + \rho_2} \frac{1}{h_b}. \qquad (8)$$

From (8), it is evident that while form drag is important for small bubble aspect ratios, it is the friction term that dominates the drag force late in time. In this paper, we argue that at low-density differences, the formation of Kelvin-Helmholtz rollups on the bubble-spike interface acts to reduce the friction drag term thus resulting in bubble acceleration. The K-H structures provide the rolling motion that mitigates the contact friction between bubbles and spikes, similar to the friction-reducing action of such vortical structures caused by dimples on a golf ball. Conversely, at large density differences, the Kelvin-Helmholtz instability is suppressed inertially, allowing the bubbles to stay terminal.

We now proceed to give a formal treatment to the ideas suggested above. Firstly, the density effect on the linear and nonlinear growth of a shear layer is described here through 2D numerical simulations. The calculations were performed using RTI-3D in a square domain (λ x λ), with periodic boundary conditions in the horizontal direction, and no-flux conditions in the direction of the velocity gradient. A velocity interface is established along the center of the domain, while the streamfunction is perturbed with a single wavelength. The velocity contrast between the two streams of fluid is spread over three numerical zones, corresponding to a piecewise linear velocity profile, while also ensuring the lengthscale of velocity variation is small in comparison to the perturbation wavelength. The shear velocities were chosen to be $\pm$ 1 m/s. A sharp density contrast is superimposed on this background condition, and both positive and negative Atwood numbers were studied. Since, in the Rayleigh-Taylor flow, the shear force between

bubbles and spikes and the buoyancy force driving the flow are orthogonal, our 2D shear calculations could be performed in the absence of gravity.

The top panel in figure 6 shows volume fraction contours at A = 0, 0.5 and 1 respectively. It is necessary for our objectives to distinguish between the presence of vorticity with the formation of a vortex core in such flows (for instance, there is considerable vorticity at A = 1 due to the large shear between the fluid streams, but no vortex). It is a K-H vortex (and not vorticity alone) that causes drag-reduction in RT flows due to its rolling motion, and the resultant bubble acceleration. We use the definition of [24] who identify connected regions with two negative eigenvalues of the velocity gradient tensor, as a vortex. In other words, if $\lambda_1 \geq \lambda_2 \geq \lambda_3$ are the three eigenvalues of S^2+D^2, where S and D are the symmetric and antisymmetric components of the velocity gradient tensor, then a vortex core is a region with $\lambda_2 < 0$. This definition ensures that a vortex is a region of a pressure minimum while eliminating factors that cause false positives due to (a) unsteady straining and (b) viscous effects.

Contours of $\lambda_2 < 0$ are shown in the bottom panels of figure 6, and clearly demonstrate the presence of vortical structures at A = 0 and 0.5, but none at A = 1. As the flow is allowed to evolve later in time, the high-speed kinks observed in figure 6 (f) are trapped in the low-speed stream (and vice-versa) and are convected along with the slow-moving fluid. However, this happens late in time, is clearly a nonlinear effect, and does not result in the formation of vortex cores at A = 1. In contrast, the vortex cores observed in figures 6 (d) and (e) are the result of Kelvin-Helmholtz overturning early in time. Both the A =0

and A = 1 cases were repeated with higher values of shear (2x and 4x). It was found that while the growth rate of the low density contrast cases scaled with ΔU, the infinite density difference case showed no variation with the velocity difference.

The growth rates of the shear layers in figure 6 may be quantified by the amplification of the r.m.s vertical velocity fluctuations $\langle v'^2 \rangle / \langle v'^2_0 \rangle$ at the interface between the two fluids. Figure 7 (a) is a semi-logarithmic time history plot of the amplification of velocity fluctuations at different density differences, and shows a consistent decay with increasing density contrasts. The late-time amplification observed for A = 1, is a result of the nonlinear effect described above, and must be distinguished with the early onset of amplification seen in the other cases.

Growth rates deduced from 7 (a) are shown in figure 7 (b) as a function of the Atwood number. The linear stability analysis of [4] considers normal modes of the form $exp\ i(k_x x+k_y y+c_i t)$, and obtains for the imaginary part of the growth rate, c_i, in the absence of surface tension and gravity,

$$c_i = \pm\sqrt{-k_x^2 (\Delta U)^2 \frac{\rho_1 \rho_2}{(\rho_1 + \rho_2)^2}}\,. \qquad (9)$$

The negative root of (9) results in exponential growth of perturbations, and shows good agreement with the numerically obtained growth rates in figure 7 (b). Note that [4] considered a sharp velocity interface, while the numerical simulations were initialized with a piecewise linear velocity profile. However, care was taken to ensure that $k_x L << 1$, where L is the initial spread of the shear layer. In figure 7 (b), we also compare the large-

Reynolds number result of [25], who used a tangent hyperbolic initial velocity profile. Note that some calculations were also repeated with a reversal of the density gradient, which yielded growth rates identical to the standard cases, consistent with the symmetry of (9) with respect to ρ_1 and ρ_2.

We now revisit the 3D single-mode Rayleigh-Taylor problem, with insight in to the behavior of density effects on Kelvin-Helmholtz instabilities. Figures 8 (a) and (b) are surfaces of $\rho = \frac{\rho_1 + \rho_2}{2}$ from the R-T calculations at A = 0.1 and 1.0 respectively, and clearly show the formation of vortical structure at low-density differences only. The realizations in figure (8) were chosen at times where the bubbles had penetrated to the same extent for both the low and high Atwood number simulations. Furthermore, our image analysis shows that at A = 1, kinks similar to those observed in figure 6 (e), form at the bubble-spike interface. For low A, the observed acceleration occurs when enough time $t_{critical}$ has passed to allow for sufficient e-foldings (n) of the Kelvin-Helmholtz instability, and this corresponds to $h_b / D_b \sim 1$. Equation (9) and figure 7 (b) suggest that for $A \rightarrow 1$, $t_{critical} = n / c_i \rightarrow \infty$. From figure 8 (b) it is also clear that for low A, c_i is only weakly dependent on A, and thus $t_{critical}$ is roughly constant. This explains why the onset of acceleration is at $h_b / D_b \sim 1$.

Figure (9) shows the time history of the percentage volume of the computational domain, that is occupied by vortices (identified through the condition $\lambda_2 < 0$), for A = 0.005 and

1.0. The low Atwood number simulation shows a dramatic increase in this quantity close to $h_b/D_b \sim 1$, while the $A = 1$ case shows no such trend.

V. Summary

Numerical simulations of the 3D single-mode RT problem in a long square duct using four codes, has revealed the surprising phenomena of late-time acceleration and likely approach to a higher Froude number. The unsteadiness can be observed elsewhere in numerical simulations[20,21,22], but not in experiments[14], which were performed, in a different regime. The critical parameter determining transition from a terminal velocity to acceleration is the bubble aspect ratio h_b/D_b. For $h_b/D_b \leq 1$, potential flow theory[6] and drag-buoyancy models[5] accurately predict bubble (and spike) terminal velocities, confirmed by our numerical simulations. For $h_b/D_b \geq 1$, secondary instabilities in the form of Kelvin-Helmholtz rollups appear, reducing the contact friction between bubbles and spikes, thus causing acceleration of bubbles. For large aspect ratios, friction drag dominates in the drag-buoyancy equation, and is reduced by the vortex structures. The numerical simulations also show that this bubble acceleration is first delayed at high A, and ultimately vanishes for $A \rightarrow 1$. This is consistent with the inertial stabilization of K-H at large density differences, predicted by linear stability analysis[4], and our 2D simulations. Using images and a vortex identification scheme, we demonstrate a high degree of correlation between the maturation of secondary instabilities and the observed change in bubble/spike behavior. We conclude that the potential flow and drag-buoyancy models remain valid in the absence of secondary vortex structures, early in time, and at high density differences.

Acknowledgements

PR and GD thank Malcolm J. Andrews for permitting use of his computer program. The work at the Los Alamos National Laboratory was performed under the auspices of the U.S. Dept. of Energy (D.O.E) under contract no. W-7405-ENG-36. AC acknowledges support from the U.S. Department of Energy under Grant No. B523820 to the Center for Astrophysical Thermonuclear Flashes at the University of Chicago. The FLASH software used in this work was developed in part by the DOE-sponsored ASC/Alliance Center for Astrophysical Thermonuclear Flashes at the University of Chicago. The PARAMESH software used in this work was developed at the NASA Goddard Space Flight Center under the HPCC and ESTO/CT projects.

References

1. Lord Rayleigh, *Scientific Papers II* (Cambridge University Pres, Cambridge, England, 1900); G.I. Taylor, Proc. R. Soc. London, Ser. A **201**, 192 (1950).
2. J.D. Lindl, *Inertial Confinement Fusion: The Quest for Ignition and Energy Gain using Indirect Drive* (AIP, Woodbury, NY 1998).
3. S.F. Gull, Mon. Not. R. Astron. Soc. **171**, 263 (1975).
4. S. Chandrasekhar, *Hydrodynamic and Hydromagnetic Stability* (Oxford University Press, Oxford, 1961).
5. D. Oron et al., Phys. Plasmas **8**, 2883 (2001).
6. V.N. Goncharov, Phys. Rev. Lett. **88**, 134502 (2002).
7. P. Ramaprabhu and Guy Dimonte, Phys. Rev. E **71**, 036314 (2005).
8. Guy Dimonte, Phys. Rev. E **69**, 056305 (2004).
9. J. Glimm *et al.*, Phys. Fluids **A 2**, 2046 (1990).
10. D. Shvarts *et al.*, Phys. Plasmas **2**, 2465 (1995).
11. Guy Dimonte, Phys. Plasmas **7**, 2255 (2000).
12. R. S. Scorer, J. Fluid Mech. **2**, 583 (1957).
13. R.M. Davies and G.I. Taylor, Proc. R. Soc. London, Ser. A **200**, 375 (1950).
14. J.T. Waddell, C.E. Niederhaus, and J.W. Jacobs, Phys. Fluids 13, 1263 (2001).
15. Guy Dimonte et al., Phys. Fluids **16**, 1668 (2004).
16. M.J. Andrews, Int. J. Numer. Methods Fluids **21**, 205 (1995).
17. B. Fryxell *et al.*, Astrophys. J., Suppl. Ser. **131**, 273 (2000); A. C. Calder *et al.*, Astrophys. J., Suppl. Ser. **143**, 201 (2002).
18. Prometheus reference

19. P. MacNiece, K.M. Olson, C. Mobary, R. deFainchtein and C. Packer, Comp. Phys. Comm., **126**, 330 (2000).

20. J.Glimm, X.L. Li and A-D. Lin, Acta Math. Appl. Sinica **18**, 1 (2002).

21. Y-N. Young et al., J. Fluid Mech. **447**, 377 (2001).

22. N.N. Anuchina *et al.*, J. Comp. and Appl. Math. **168**, 11 (2004).

23. Fluid Dynamic drag – Horner

24. J. Jeong and F. Hussain, J. Fluid Mech. **285**, 69 (1995).

25. R. Betchov and A. Szewczyk, Phys. Fluids **6**, 1391 (1963).

	Governing equations	AMR	Surface tension	Compressible
RTI-3D	Euler	No	No	No
FLASH	Euler	Yes	No	Yes
NAV/STK	Navier-Stokes	Yes	Yes	No
PROMETHEUS	Euler	No	No	Yes

Table 1. Description of numerical codes used in this study.

	Atwood number	Perturbation Wavelength (cm)	Gravity (cm/s^2)	Resolution
RTI-3D	0.005 0.1 0.25 0.5 0.75 0.9	10.0	2.0	32x32x256
FLASH	0.1 0.25 0.5 0.9	0.25	1.0	6 (AMR)
NAV/STK	0.1 0.2 0.3 0.4 0.5 0.6 0.7 0.8 0.9	1.0	1.0	? (AMR)
PROMETHEUS	0.5	0.25	1.0	60x720

Table 2. Simulation parameters used in this study.

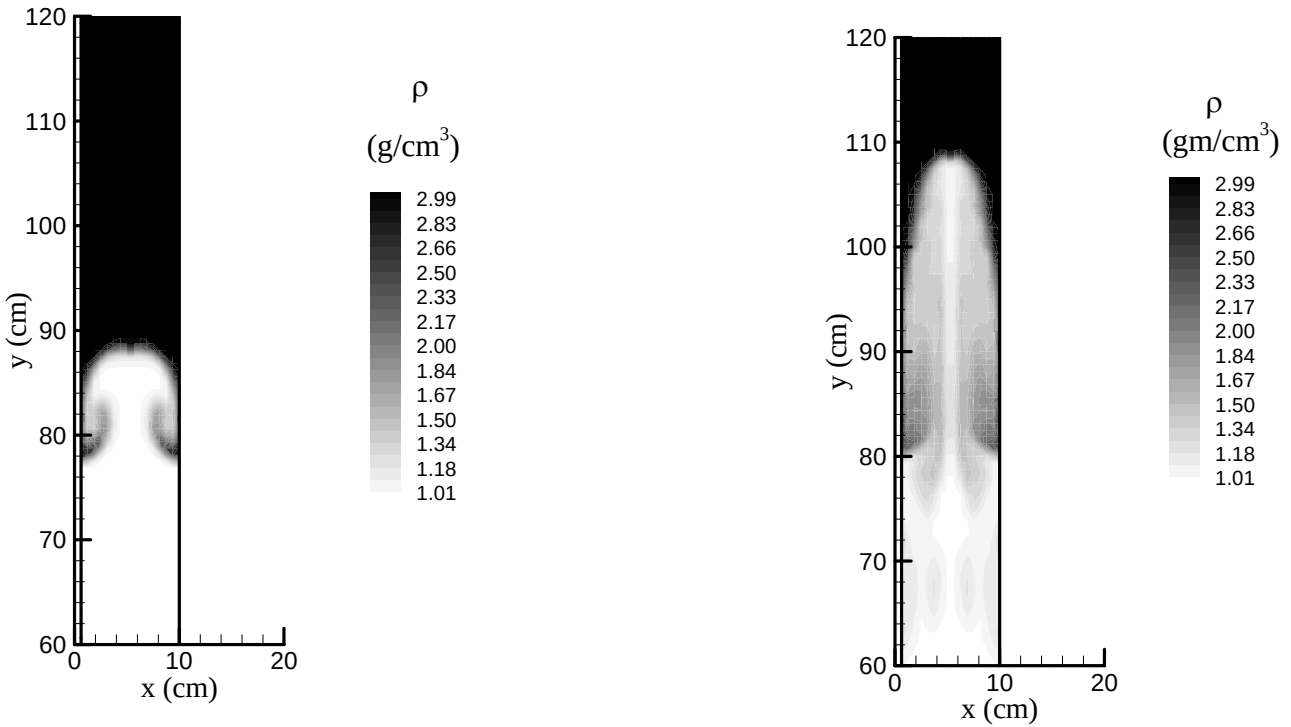

(a) (b)

Figure 1. Images of bubble-front at early-time (during terminal velocity) and late-time (acceleration stage) from RTI-3D. A = 0.5. Location of original interface is at y = 80cm.

(a) (b)

Figure 2. Images of bubble-front at early-time (during terminal velocity) and late-time (acceleration stage) from DNS. A = 0.2. Location of original interface is at y = 4 cm.

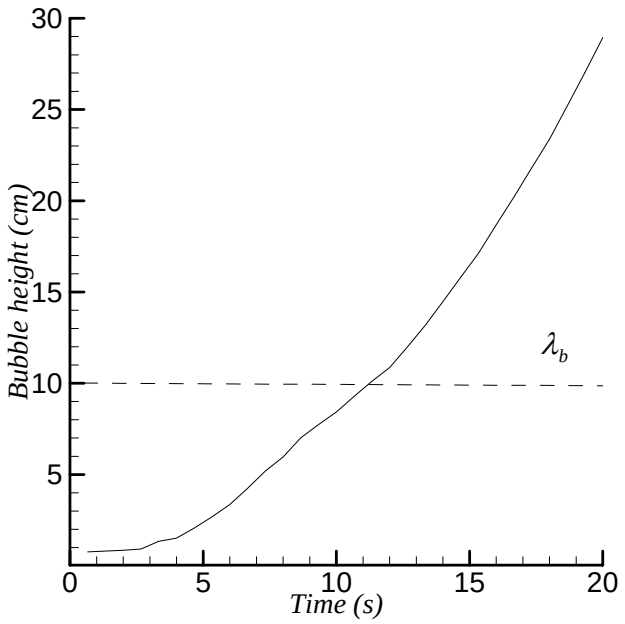

(a)

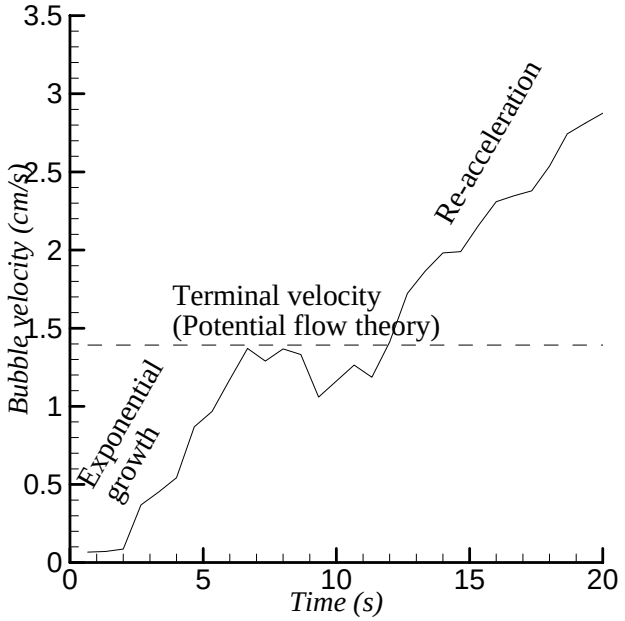

(b)

Figure 3. Time-histories of (a) bubble penetration and (b) bubble velocity showing distinct stages of single-wavelength bubble growth. Results shown are from RTI-3D at A = 0.5. The dashed line in (a) represents the bubble wavelength λ_b, beyond which the re-acceleration is observed. The terminal velocity from potential flow theory is included in (b) for comparison.

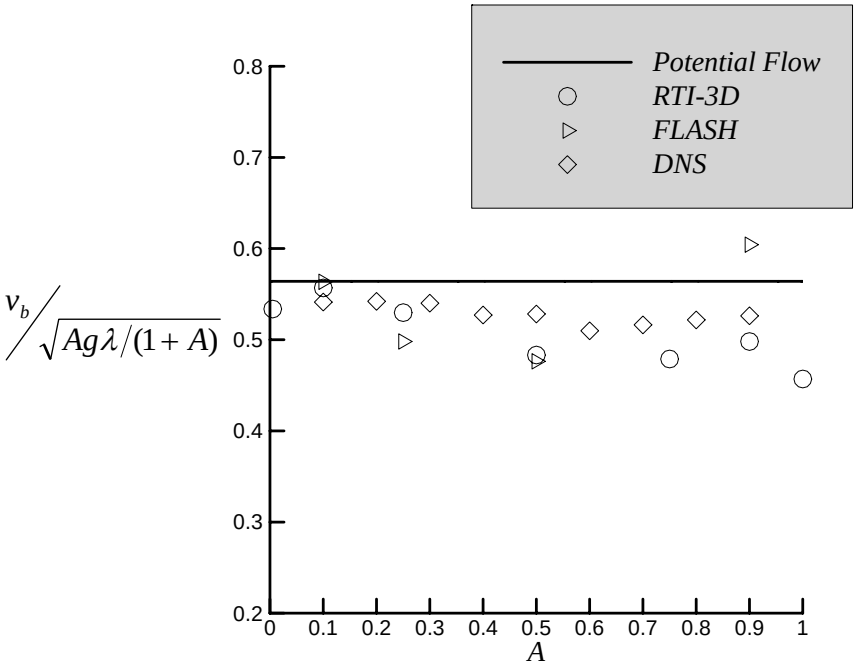

Figure 4. Bubble Froude number ($v_b / \sqrt{Ag\lambda/(1+A)}$) for $h_b / D_b < 1$ at different Atwood numbers from numerical simulations and potential flow theory[6].

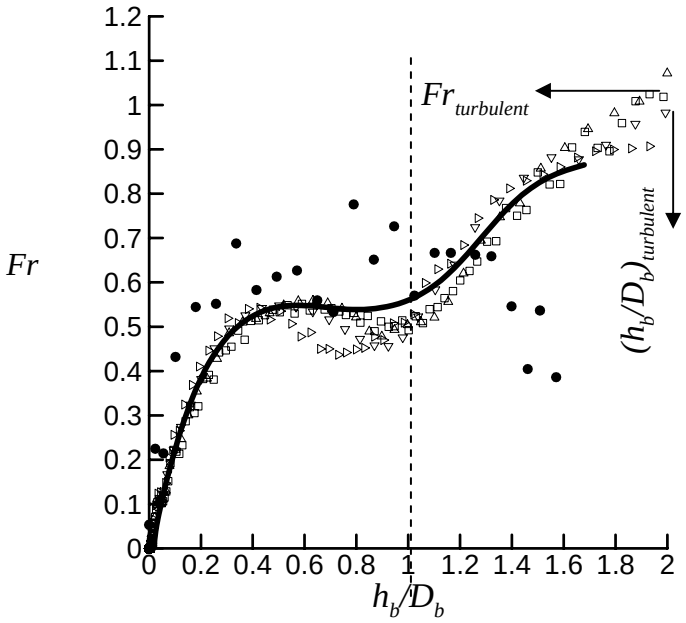

Figure 5. Froude number ($v_b / \sqrt{Ag\lambda/(1+A)}$) vs. h_b / D_b from numerical simulations. Hollow symbols represent MILES, while the solid line indicates DNS. All calculations are for $A \leq 0.5$ and show onset of bubble acceleration at $\frac{h_b}{D_b} \sim 1$. Solid symbols denote high Atwood number result.

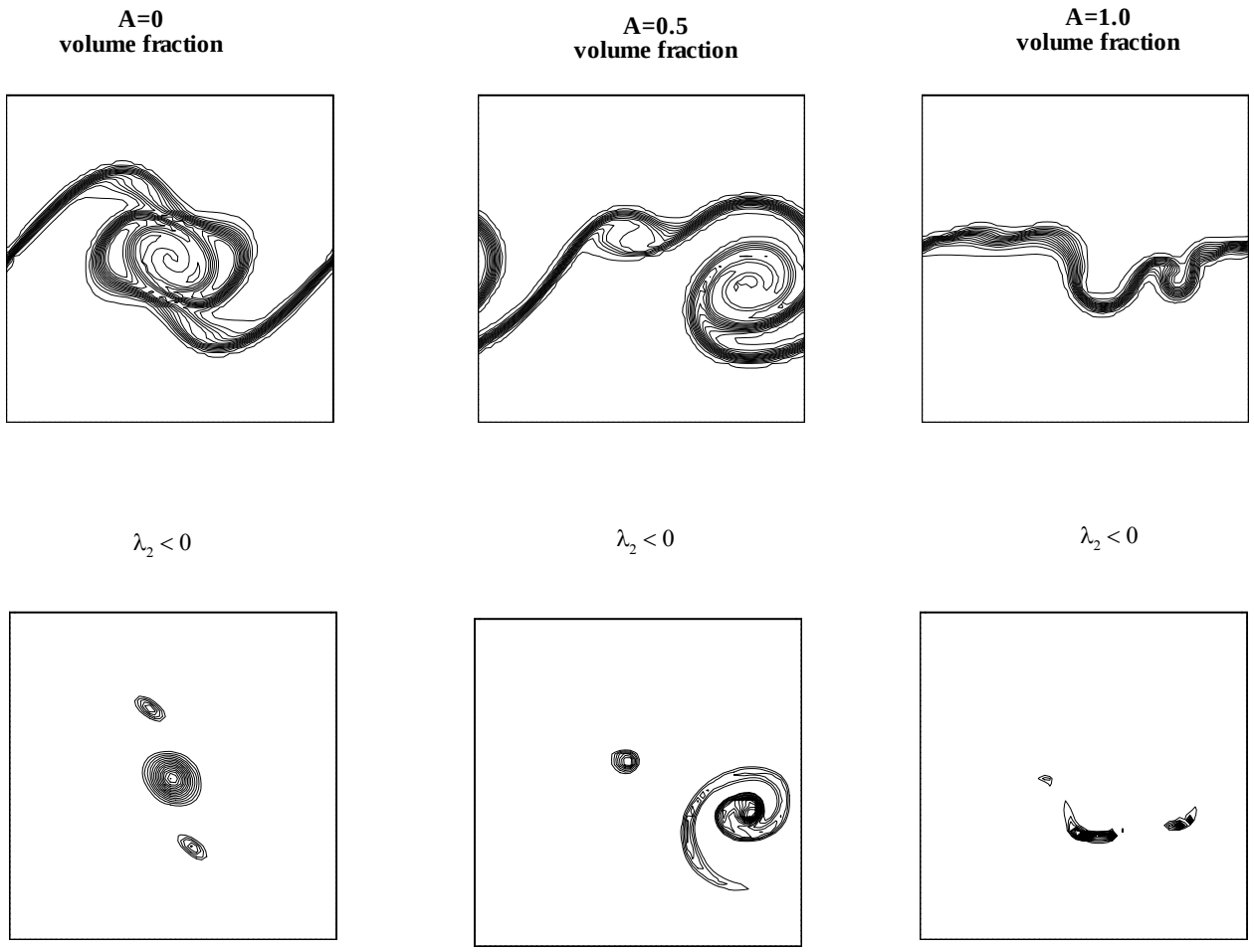

Figure 6. Contours of volume fraction (top row) and negative second eigenvalue (bottom row) from 2D NS of a plane shear layer.

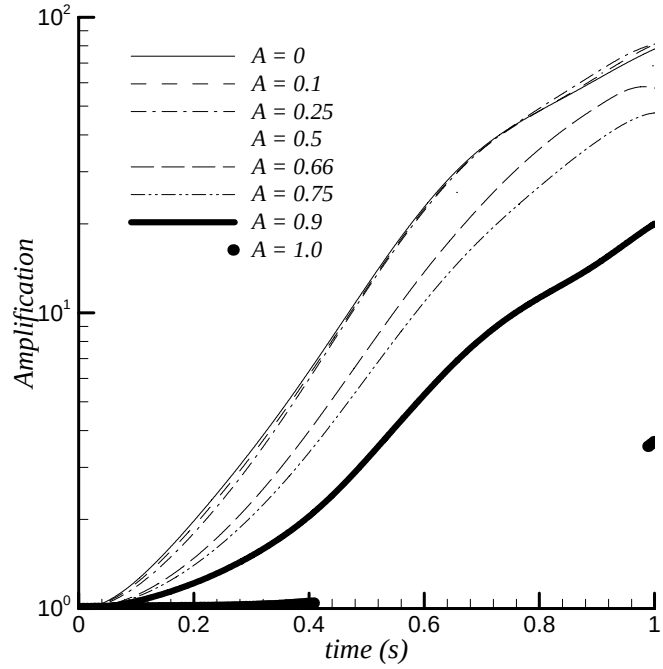

(a)

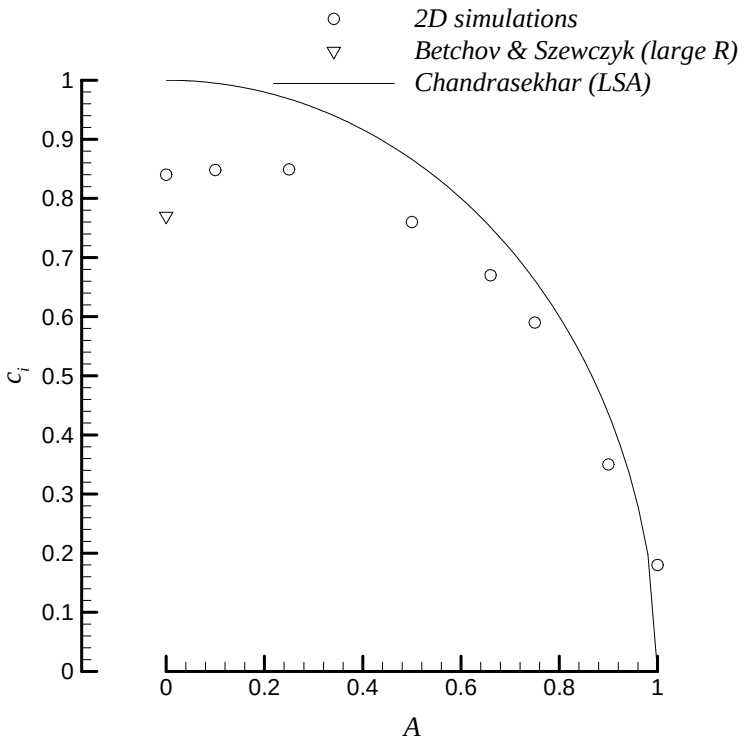

(b)

Figure 7 (a). Amplification of centerline velocity fluctuations for the Kelvin-Helmholtz problem at different density differences and (b) the corresponding growth rates c_i as a function of A.

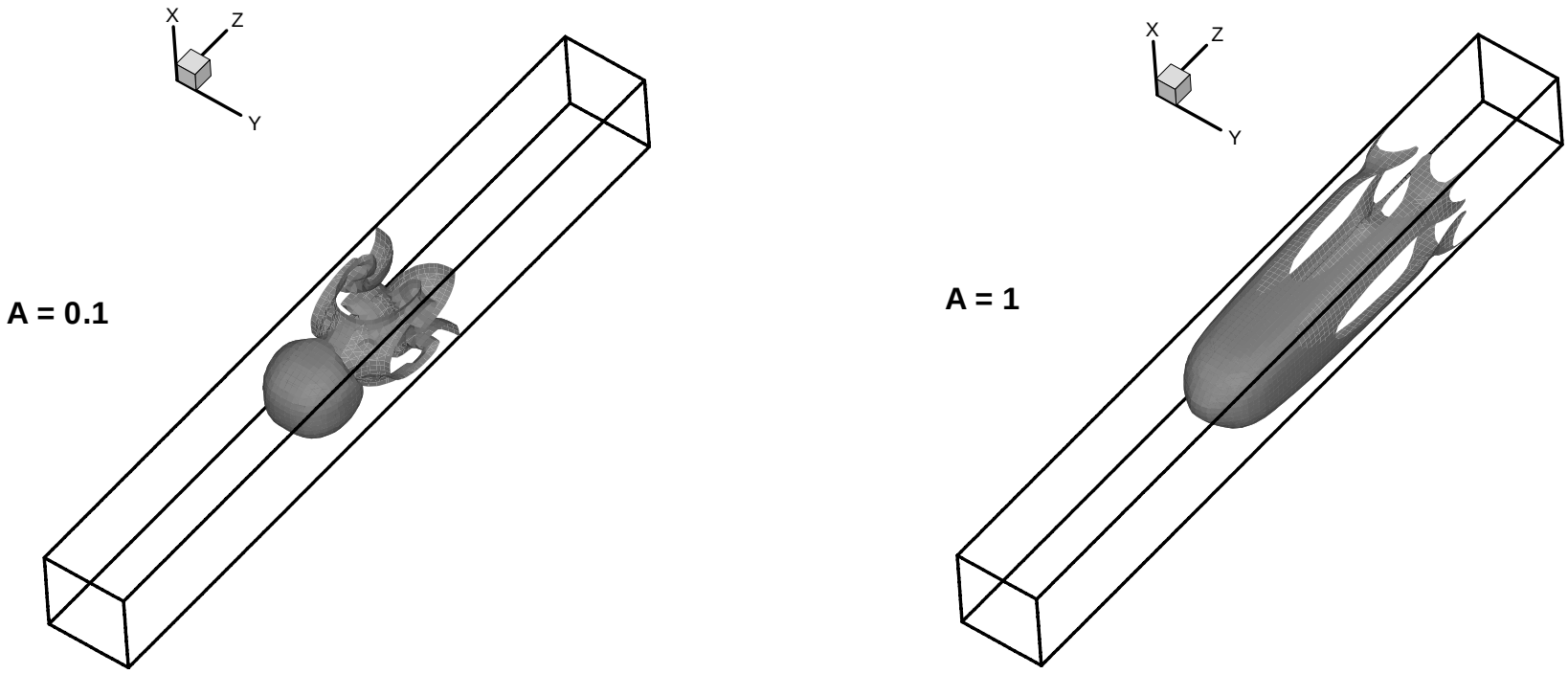

(a) (b)

Figure 8. Iso-surfaces of volume fraction (=0.5) from the single-mode Rayleigh-Taylor calculations at A = 0.1 (a) and A = 1 (b).

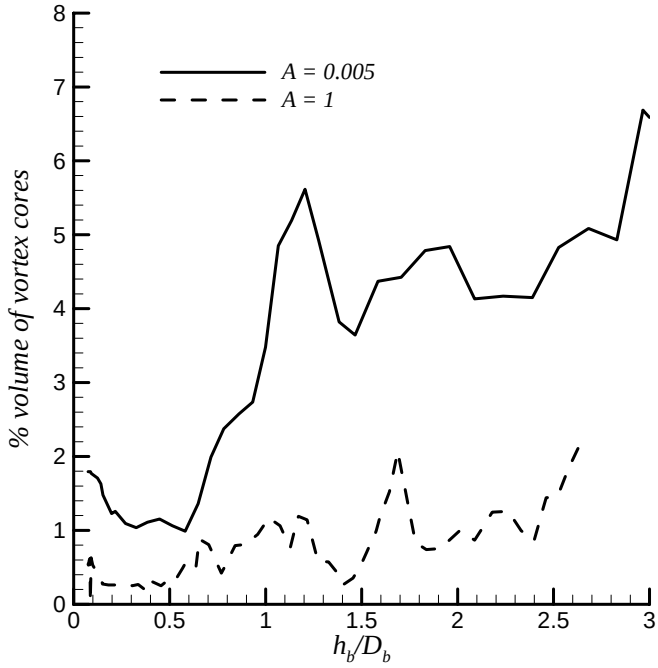

Figure 9. Variation of vortex core size at A = 0.005 and A =1 with the bubble aspect ratio.